Joint Polar Satellite System (JPSS) Ground Project

Joint Polar Satellite System (JPSS) Advanced Technology Microwave Sounder (ATMS) SDR Calibration Algorithm Theoretical Basis Document (ATBD)

For Public Release

Center for Satellite Applications and Research
College Park, Maryland

National Oceanic and
Atmospheric
Administration

This page intentionally left blank.

Joint Polar Satellite System
Advanced Technology Microwave Sounder (ATMS)
SDR Radiometric Calibration
Algorithm Theoretical Basis Document (ATBD)

JPSS Electronic Signature Page

Prepared By:

JPSS ATMS SDR Science Team
(Electronic Approvals available online at http://www.star.nesdis.noaa.gov/jpss/ATBD.php)
Point of Contact/Custodian: Fuzhong Weng (Fuzhong.Weng@noaa.gov),

Approved By:

JPSS Ground System

Eric Gottshall (Eric.Gottshall@noaa.gov)
DPA IPT Lead/Algorithm Engineering Review Board (AERB) Chair
JPSS Ground Project

Lihang Zhou (Lihang.Zhou@noaa.gov)
DPA IPT Deputy-Science/Algorithm Engineering Review Board (AERB) Co-Chair
NOAA/NESDIS/STAR

Arron L. Layns (Arron.Layns@noaa.gov)
DPA IPT Deputy-Integration
NOAA/NESDIS/NJO

Center for Satellite Applications and Research
College Park, Maryland

This page intentionally left blank.

Change History Log

Center for Satellite Applications and Research National Center for Weather and Climate Prediction College Park, Maryland				
Revision/Change Record			**For Document No.** **JPSS ATBD #1**	
Revision	**Document Date**	**Revision/Change Description**		**Pages Affected**
Baseline	27 Jan 2010	Public Released version		All
Version 1	18 Dec 2013	Modified baseline version with the following additions from Suomi NPP cal/val: TDR to SDR conversion theory for scan angle bias correction, resampling SDR theory, striping analysis and lunar intrusion correction.		All

This page intentionally left blank.

Table of Contents

Acronyms

ADC	Analog-to-digital converter
AIRS	Atmospheric Infrared Sounder
AMSU	Advanced Microwave Sounding Unit
ARM	Atmospheric Radiation Measurement program
ATBD	Algorithm Theoretical Basis Document
ATMS	Advanced Technology Microwave Sounder
ATOVS	Advanced TOVS
CDR	Climate Data Record
CrIMSS	Cross-track Infrared and Microwave Sounding Suite
CrIS	Cross-track Infrared Sounder
DN	Data number
EDR	Environmental Data Record
EDU	Engineering Development Unit
EOS	Earth Observing System
EOSDIS	EOS Data and Information System
EU	Engineering unit
FRD	Functional Requirements Document
GSFC	Goddard Space Flight Center
HAMSR	High Altitude MMIC Sounding Radiometer
HIRS	High resolution Infrared Radiation Sounder
IF	Intermediate frequency
IMAS	Integrated Multispectral Atmospheric Sounder
IPO	Integrated Program Office
IORD	Integrated Operational Requirements Document
IR	Infrared
JPL	Jet Propulsion Laboratory
LO	Local oscillator
MHS	Microwave Humidity Sounder
MIT	Massachusetts Institute of Technology
MMIC	Monolithic Microwave Integrated Circuit
MSU	Microwave Sounding Unit
MUX	Multiplexer
MW	Microwave
NASA	National Aeronautic and Space Administration
NEDT	Noise-equivalent delta-T
NGES	Northrop Grumman Electronic Systems
NGST	Northrop Grumman Space Technologies
NOAA	National Oceanic and Atmospheric Administration
NPOESS	National Polar-orbiting Operational Environmental Satellite System
NPP	NPOESS Preparatory Project
NWP	Numerical Weather Prediction
NWS	National Weather Service
ORD	Operational Requirements Document
PLLO	Phase locked local oscillator

POES	**P**olar-orbiting **O**perational **E**nvironmental **S**atellite
POS	**P**erformance and **O**perations **S**pecification
PRT	**P**latinum **r**esistance **t**hermometer
QA	**Q**uality **a**ssessment
QC	**Q**uality **c**ontrol
RDR	**R**aw **D**ata **R**ecord
RF	**R**adio **f**requency
SDR	**S**ensor brightness temperature **D**ata **R**ecord
SSMIS	**S**pecial **S**ensor **M**icrowave **I**mager/**S**ounder
SSM/T	**S**pecial **S**ensor **M**icrowave **T**emperature sounder
TDR	Antenna brightness **T**emperature **D**ata **R**ecord
TIROS	**T**elevision **I**nfrared **O**bservation **S**atellite
TOVS	**T**IROS **O**perational **V**ertical **S**ounder
WMO	**W**orld **M**eteorological **O**rganization

1. Introduction

This ATMS Algorithm Theoretical Basis Document (ATBD) describes the theoretical basis and, to a limited extent, the implementation of algorithms used for converting raw data numbers (DN) or engineering units (EU) from the telemetry of the ATMS instrument, which are contained in the Raw Data Records (RDR), to calibrated brightness temperatures contained in the Sensor Data Records (SDR). The RDRs are raw and minimally processed telemetry, which are the input to the SDR process. The output from the SDR process serves as the input to the Environmental Data Record (EDR) process, where the calibrated radiances from CrIS and calibrated brightness temperatures from ATMS are converted to geophysical parameters through a "retrieval" process.

The algorithms described in this document are very similar to those that have been developed by NOAA and NASA for the AMSU-A and -B instruments, which have flown since 1998 (NOAA) and 2002 (NASA), respectively. Details of the description are based on preliminary software developed by the ATMS contractor, NGES, and delivered in mid-2004 as version 2.2. Although the basic functionalities and principles of operation of these instruments are quite similar, there are minor differences between the respective algorithmic approaches. For example, while NOAA prefers to convert radiometer measurements to physical radiance (unit: mW/m^2-sr-cm^{-1}), the Suomi NPP mission iemploys an approach to convert radiometer measurements to brightness temperatures (unit: K).

Although it is intended that this ATBD be readable as a standalone document, it is recommended that the reader references the related instrument and system description documents available from NGES (Anderson, 2004) and the 2013 special issue of Journal of Geophysical Research Atmosphere on Suomi NPP Satellite Calibration, Validation and Applications. There is a brief description of the instrument itself and an explanation of references to devices, procedures and tables used by the SDR algorithms. However, for a full understanding of the hardware and the measurement system, the reader should also refer to the CrIS SDR ATBD, the CrIMSS EDR ATBD, and the respective JPSS Level-1 Requirements Documents. The present document reflects as-built performance characteristics to the extent they are known, and otherwise assumes full compliance of the hardware with the specifications.

This document describes the functions performed by the ground data system. However, it should be noted that nothing should be implied about the architecture or the implementation of the system. Thus, algorithms that may be described here as if they were to be executed in conjunction with each other could in fact be executed in isolation from each other. For example, data quality checking belonging to individual steps may be consolidated and executed before those step are reached in the actual processing system in order to provide an efficient implementation. Also, in some instances there may be essential elements missing from the software implementation. These will be noted in the text and in a companion commentary.

2. Historical Perspective

The Advanced Technology Microwave Sounder (ATMS), together with the Crosstrack Infrared Sounder (CrIS) — a high spectral resolution IR spectrometer, are designed to meet the weather requirements for National Oceanic and Atmospheric Administration (NOAA) and climate research objectives of the National Aeronautics and Space Administration (NASA). The first version of this Crosstrack Infrared Microwave Sounding Suite (CrIMSS) is on Suomi National Polar-Orbiting Partnership (SNPP) mission and subsequently on a series of Joint Polar Satellite System (JPSS) mission.

The High Resolution Infrared Sounder (HIRS) and the Microwave Sounding Unit (MSU), together form the TIROS Operational Vertical Sounder (TOVS) on the NOAA polar orbiting environmental satellite system (POES) and have supported the National Weather Service (NWS) forecasting effort with global temperature and moisture soundings since the late 70's. In the course of the years HIRS has been periodically upgraded, and a jump from MSU to the Advanced Microwave Sounding Unit (AMSU) was made in 1998. The combined HIRS/AMSU system is called the Advanced TOVS (ATOVS) and has been the backbone of the NOAA POES systems.

During the mid-1980's, while TOVS was still flying, it was determined that future numerical weather prediction (NWP) would soon require satellite sounders with accuracies equivalent to or better than radiosondes. NASA thus launched an effort to develop the technology and capability to achieve this requirement. The result was the Atmospheric Infrared Sounder (AIRS), which, together with an AMSU microwave suite, was launched as part of the Aqua mission in 2002. AIRS is the first of a subsequent series of high spectral resolution IR sounders, and has already demonstrated its utility as a radiosonde-quality satellite sounding instrument. AIRS data is operationally assimilated by a number of NWP centers and has resulted in significant positive impacts on global medium range forecasts. Although using a Fourier transform spectrometer, which is an approach different from AIRS's grating spectrometer, CrIS is the successor of AIRS and has a comparable performance as AIRS. Other instruments in the same class such as Infrared Atmospheric Sounding Interferometer (IASI) are deployed elsewhere on METOP satellites.

During the mid-1990's, while AIRS was being built, an effort was made by NASA to transfer the AIRS technology to NOAA operations, with the goal of providing an AIRS follow-on instrument for the NPOESS (now JPSS) missions. A technology development effort was launched,with a primarily focus on reducing the mass, size and power consumption of the microwave component of the sounding suite this time. The proposed system was called the Integrated Multispectral Atmospheric Sounder (IMAS) – a single combined infrared and microwave instrument that was intended to fly as a demonstration on the NASA New Millennium Program's EO-3 mission. The effort was terminated in mid-1998 largely due to cost constraints, but many of the IMAS microwave specifications were later adopted for the ATMS instrument.

It was initially the intention to use the 118-GHz oxygen line for temperature sounding in the IMAS system, instead of the 50-60 GHz band used by AMSU. This would make it possible to shrink the aperture by a factor of more than two (and therefore also the overall mass and size) while maintaining spatial resolution and other performance measures. A field of view (FOV) of the same size as the IR sounder (i.e. 1.1°) was highly desired, and the IMAS/MW component

was therefore designed to have this beam width for all sounding channels (i.e. in the 118-GHz band for temperature sounding and in the 183-GHz band for water vapor sounding). Later, it was realized that even the most transparent 118-GHz channels may not be able to penetrate the atmosphere to the Earth surface under very humid and cloudy conditions (e.g., in the tropics). The 50-GHz band will then be restored to provide backup capabilities for such situations. A compromise was made to use the same aperture size at 50 GHz as at 118 GHz, and a 2.5° beam width. The IMAS team also determined that the microwave instrument should have the same spectral channels as AMSU for "science continuity" and that a few additional channels were desirable. As a result, two new channels were suggested to be added in the 183-GHz band, and one new window channel be added in the 50-GHz band. In addition, the 150-GHz quasi-window channel used in AMSU-B was replaced with one at 166 GHz, which can be operated as part of an advanced-technology of the 183-GHz receiver (thus saving one receiver chain). These were considerations provided by the AIRS team. Most of these specifications and characteristics are now part of the ATMS specifications except for the 118-GHz band which was eliminated early in the program due to cost constraints, and 2.5° beam width which was improved to 2.2°.

The most significant advance under IMAS was the development of monolithic microwave integrated circuit (MMIC) technology at sounding frequencies (i.e. at 50, 118 and 183 GHz), which allows for sensitive and compact receivers and spectrometers. Such a technology was previously only available at considerably lower frequencies, Sample receivers and compact solid-state filter banks were developed for the two lower frequency bands, and low noise amplifiers (i.e. precursors to full receivers) were developed for the 183-GHz band. After the termination of IMAS these technological items were incorporated into an aircraft-based microwave sounder called the High Altitude MMIC Sounding Radiometer (HAMSR),developed under the NASA Instrument Incubator Program. HAMSR may be viewed as an ATMS precursor as a prototype of ATMS in many respects. HAMSR uses a dual aperture with two reflectors operating on a common axis, which was adopted for ATMS. HAMSR has been successfully operated on the NASA ER-2 high altitude aircraft since 2001. In summary, ATMS has heritage primarily from AMSU, the IMAS design and the HAMSR.

3. Instrument Description

In this section we give a brief description of the ATMS instrument. ATMS instrument layout is
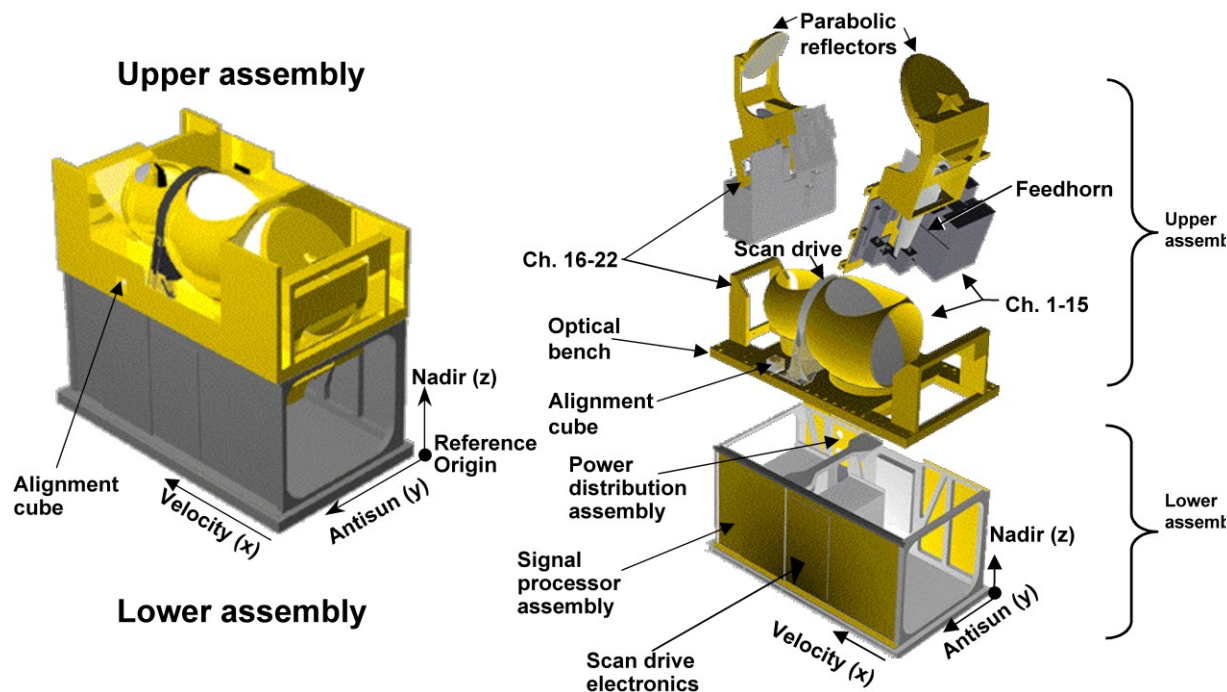
Figure 1. ATMS instrument layout

illustrated in Fig. 1. ATMS is a 22-channel microwave sounder providing both temperature soundings between the surface and the upper stratosphere (i.e. to about 1 mb, at an altitude of about 45 km) and humidity soundings between the surface and the upper troposphere (i.e. to about 200 mb, at an altitude of about 15 km). Like AMSU, it is a crosstrack scanner. There are two receiving antennas — one serving 15 channels below 60 GHz with a beam width of 2.2° except for the lowest two channels and the other serving seven channels above 60 GHz with a beam width of 1.1° except for the lowest channel. The antennas consist of plane reflectors mounted on a scan axis at a 45° tilting angle, so that radiation from a direction perpendicular to the scan axis is reflected into a direction parallel to the scan axis (i.e. a 90° reflection). With the scan axis being oriented in the along-track direction, this results in a cross-track scanning pattern. The reflected radiation is then focused by a stationary parabolic reflector onto a dichroic plate, and finally either reflected to or passed to a feedhorn. Each of the two aperture/reflector serves two frequency bands to cover a total of four bands.In other words, radiation from a direction within the scan plane, which depends on the angle of rotation of the reflector, is reflected and focused onto the
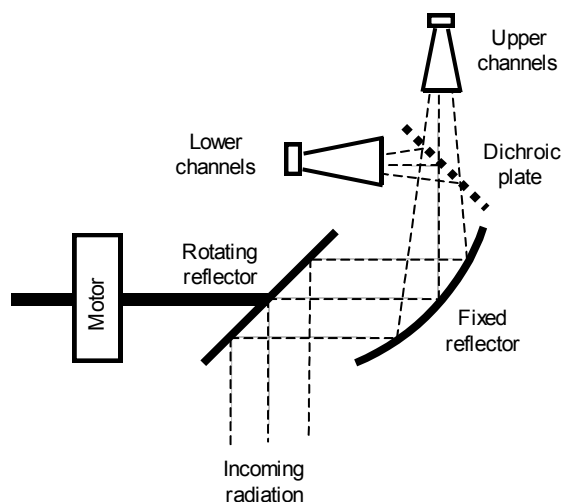
Figure 2. ATMS antenna and RF feed subsystem (schematically); one of two

receiver apertures, which are conical feedhorns. A schematical illustration of ATMS antenna and RF feed subsystem is provided in Fig. 2.

The The ATMS antenna system is designed such that a slightly diverging conical pencil "beam" is formed with a half-power width (also called the 3-dB width) of being either 1.1°, 2.2° or 5.2°, with a possible variation being within ±10% from channel to channel. Each beam is approximately Gaussian-shaped at the center and receives a significant portion of its energy outside the half-power cone. Approximately 95-97% of the energy is received within the so-called main beam, which is defined as 2.5 times the half-power beam width, i.e., the ATMS "main beam" is either 2.75°, 5.5° or 13° wide. A significant amount of energy (i.e. up to 5%) is thus received from outside the main beam. Figure 3 shows a typical antenna pattern. The pattern in the vicinity of the main beam is called the near sidelobes, while that further away is called the far sidelobes. The far sidelobes contribute significantly to the measurement errors.
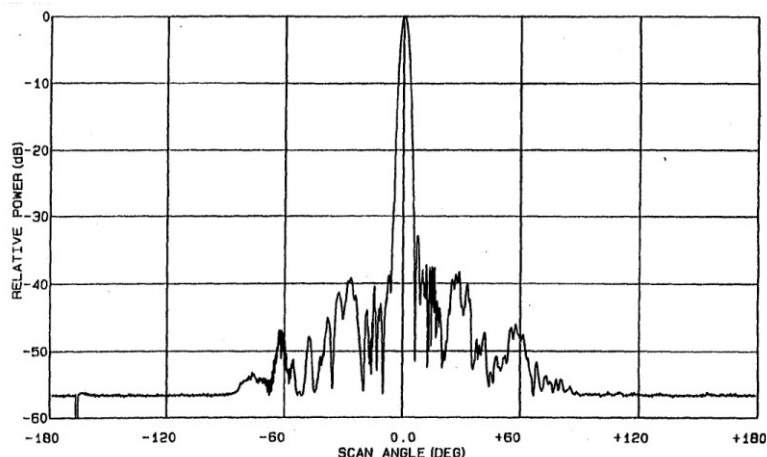
Figure 3. Typical microwave antenna pattern

For some bands, the feedhorn is followed by a diplexer that splits the RF energy into two parallel signal paths that proceed to the respective receiver, which is in most cases a heterodyne system. Each sub-band is further converted by a mixer, separated into channels with filters, and finally detected. Figure 4 shows a block diagram of the ATMS system. Discussions on various
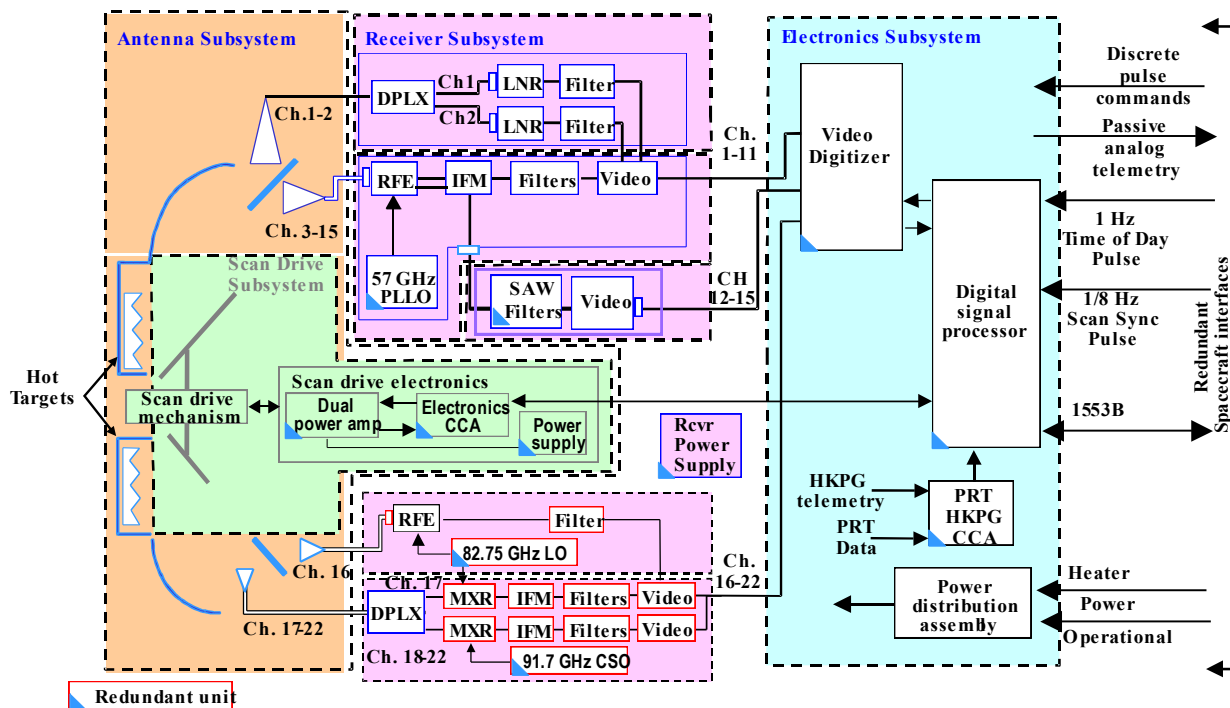

Figure 4. ATMS block diagram

signal paths that lead to the individual spectral channel outputs are provided below.

Two large apertures are used for the 15 lowest-frequency channels, which are sometimes referred to as the KAV-aperture, since it covers K-band (channel 1), Ka-band (channel 2) and V-band (channels 3-15). The dichroic plate, which reflects frequencies below a certain value and transmit those above, splits the RF energy into a low frequency path (reflected) and a high frequency path (transmitted). The output of the low frequency feedhorn enters a diplexer, which in turn splits the now somewhat band limited RF energy into two parallel paths. Each path is fed into an amplified receiver chain, followed by a bandpass filter centered either at 23.8 GHz (channel 1) or at 31.4 GHz (channel 2). These are the only non-heterodyne receivers in the ATMS system.

The output of the higher frequency feedhorn is fed into an amplified and bandpass filtered heterodyne receiver with two down-converter/mixer chains by a common local oscillator (LO) operating at 57.290344 GHz, which is a highly stable and temperature controlled crystal referenced phase locked oscillator. One path is lowpass filtered, resulting in a single-sideband intermediate frequency (IF) band located at 1.6 – 7.1 GHz below the LO frequency. This band is in turn passed through a set of signal splitters/multiplexers and bandpass filters that select channels 3-9. The other path is bandpass filtered, resulting in a double-sideband IF band located at 10 – 400 MHz away from the LO frequency. Two channels (10 and 11) are formed with conventional bandpass filters similar to those used for channels 3-9, while the remaining channels (12-15) are formed with a standing acoustic wave (SAW) filter assembly. Note that the SAW assembly is implemented as a set of four pairs of filters, each positioned symmetrically with respect to an IF frequency of 322.2 MHz. The outputs of each filter pair are combined and amplified. Channels 12-15 are therefore in effect quadruple-sideband channels.

A smaller aperture is used for the seven highest frequency channels and is sometimes referred to as the WG-aperture, since it covers W-band (channel 16) and G-band (channels 17-22). Here the lower frequency path (i.e., the signal reflected from the dichroic plate) enters a single feedhorn and an amplified highpass filtered heterodyne receiver chain, where the mixer uses an LO operating at 82.75 GHz, producing a single upper sideband IF signal that is finally put through a 4450-6450 MHz bandpass filter for channel 16 (which results in a channel located at 87.2-89.2 GHz). The high frequency path (i.e., the transmitted signal through the dichroic plate) enters a smaller feedhorn followed by a diplexer that splits the signal into two paths. One path goes to a second harmonic mixer that uses the same LO as the channel 16 receiver. The resulting double sideband IF signal is put through a 350-1500 MHz bandpass filter for channel 17, which is then located at 164-167 GHz with a gap between 165.15-165.85 GHz. The second path goes to a second harmonic mixer, which uses an LO operating at 91.655 GHz. The double sideband IF is passed through a set of filters that produce channels 18-22. These channels are therefore centered at 183.31 GHz $\pm$ Δf, where Δf is 7, 4.5, 3, 1.8 or 1 GHz, with their bandpass width varing from channel to channel.

Table 1 summarizes the performance specifications of all 22 channels, including radiometric sensitivity which is usually called noise equivalent temperature change and denoted as NEDT. It lists three frequency specifications: nominal center frequency, center frequency stability (i.e., the allowed maximum deviation from the nominal center frequency value), and specified and as-built bandwidth. All are given in MHz. The as-built bandwidth notation is "NxΔf", where N is the number of sub-bands used for a channel and Δf is the width of each sub-band. For example, 2x270 means a double-band channel with each of the two bands being 270 MHz wide.

Beamwidth is also listed in Table 1. A single linear polarization is measured for each channel. The nominal polarization direction at the nadir scan position is listed in Table 1.

Table 1. ATMS spectrometric and radiometric specifications

| Ch	RF path			Center frequency [MHz]		Bandwidth [MHz]		NEDT [K]	Pol	Beamwidth [°]	Accuracy [K]
	Ant	Feed	Rcvr	Value	Stab	Req	True	Req		Req	Req
1	A	1	a	23800	<10	<270	1x270	0.7	QV	5.2	1.0
2	A	1	b	31400	<10	<180	1x180	0.8	QV	5.2	1.0
3	A	2	c	50300	<10	<180	1x180	0.9	QH	2.2	0.75
4	A	2	c	51760	< 5	<400	1x400	0.7	QH	2.2	0.75
5	A	2	c	52800	< 5	<400	1x400	0.7	QH	2.2	0.75
6	A	2	c	53596±115	< 5	170	2x170	0.7	QH	2.2	0.75
7	A	2	c	54400	< 5	400	1x400	0.7	QH	2.2	0.75
8	A	2	c	54940	<10	400	1x400	0.7	QH	2.2	0.75
9	A	2	c	55500	<10	330	1x330	0.7	QH	2.2	0.75
10	A	2	d_1	57290.344 [f_0]	<0.5	330	2x155	0.75	QH	2.2	0.75
11	A	2	d_1	f_0±217	<0.5	78	2x 78	1.2	QH	2.2	0.75
12	A	2	d_2	f_0±322.2±48	<1.2	36	4x 36	1.2	QH	2.2	0.75
13	A	2	d_2	f_0±322.±22	<1.6	16	4x 16	1.5	QH	2.2	0.75
14	A	2	d_2	f_0±322.±10	<0.5	8	4x 8	2.4	QH	2.2	0.75
15	A	2	d_2	f_0±322.±4.5	<0.5	3	4x 3	3.6	QH	2.2	0.75
16	B	3	e	88200	<200	2000	1x2000	0.5	QV	2.2	1.0
17	B	4	f	165500	<200	3000	2x1150	0.6	QH	1.1	1.0
18	B	4	g	183310±7000	<30	2000	2x2000	0.8	QH	1.1	1.0
19	B	4	g	183310±4500	<30	2000	2x2000	0.8	QH	1.1	1.0
20	B	4	g	183310±3000	<30	1000	2x1000	0.8	QH	1.1	1.0
21	B	4	g	183310±1800	<30	1000	2x1000	0.8	QH	1.1	1.0
22	B	4	g	183310±1000	<30	500	2x 500	0.9	QH	1.1	1.0

 For a rotating main reflector, the detected polarization vector rotates as the scan reflector rotates. This can be understood by envisioning the detected polarization vector, which is fixed relative to the feedhorn and projected onto the ground below, by simple geometric imaging. The direction indicated in Table 1 as "V" corresponds to a direction that lies in the scan plane, while "H" is the direction that is perpendicular to the scan plane – i.e. in the horizontal plane. At nadir, the two polarizations are of course degenerate, i.e., the observed emissions at V and H polarizations would be identical for an isotropic surface. As the scanner rotates the beam away from nadir, the detected "V" polarization rotates out of the scan plane while the detected "H" polarization rotates out of the perpendicular plane and thus also out of the horizontal plane. The angle of rotation away from the respective planes equals the scan angle relative to nadir. This is illustrated schematically in Fig. 5, which shows the projection of the various polarization vectors in the plane perpendicular to the ray path (i.e., the plane that contains the electromagnetic field vectors). This plane coincides with the horizontal plane for the nadir scan position but rotates as the scan position changes. In addition, as explained above, the "H" and "V" polarization vectors rotate within this plane. When surface emissivity and similar quantities are computed, it is important to a correct transformation between the observed "H" and "V" vectors and the local true H and V vectors.
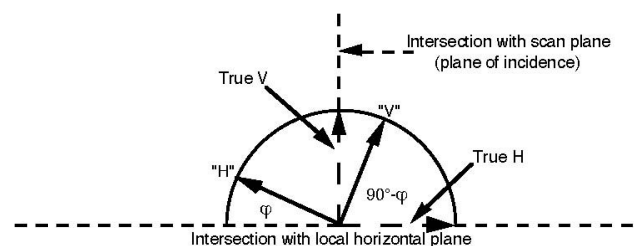
Figure 5. Polarization vectors, in the transverse plane

The antenna reflectors continuously rotate counter-clockwise relative to the direction of spacecraft motion (i.e. the spin vector points in the negative x-direction while the spacecraft moves along the positive x-direction), to complete three revolutions in eight seconds. The scan mechanism is synchronized to the spacecraft clock with a "sync" pulse every 8 seconds (i.e., for every third revolution). Each scan cycle is divided into three segments. In the first segment the earth is viewed at 96 different angles, symmetric around the nadir direction. The antenna is in continuous motion and the 96 samples are taken "on the fly", with each sample representing the mid-point of a brief sampling interval of about 18 ms. The scan speed is such that the corresponding angular sampling interval is 1.11° (i.e., the scan speed is about 61.6°/second). The angular range between the first and last sample centroids is therefore 105.45° (i.e. ±52.725° relative to nadir). The antenna then accelerates and moves to a position between the earth's limb and the spacecraft horizon to point toward an unobstructed view of space. There it resumes the same slow scan speed as it maintained across the Earth scenes to take four consecutive cold calibration measurements. Next, the antenna is again accelerated to the zenith direction to point toward an internal calibration target that is at the relatively high ambient instrument temperature. It is again slowed down to the same slow scan speed as it has while taking the Earth scenes to take four consecutive warm calibration measurements. Finally, it is accelerated to move to the starting Earth scene position, where it is slowed down to repeat another scan cycle. Every third cycle the synchronization signal arrives just before the start position is reached and is used to maintain this pattern through a phase locked loop. Figure 6 illustrates a normal operational scan mode. (There is also a stare mode, where the antenna can be pointed to the nadir direction or either of the calibration directions for an extended period of time, but that is only used for special purposes.) Each of the 96 earth samples takes about 18 milliseconds, for a total of approximately 1.73 seconds. The "duty cycle" of ATMS is therefore about 65%, i.e. about 65% of the scan cycle period is dedicated to Earth observations.
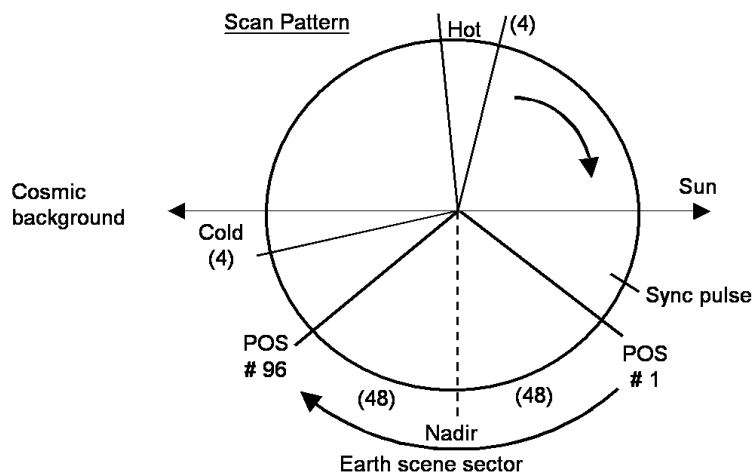
Figure 6. Scan sequence (flight direction is toward the reader)

4. Instrument Interoperability Issues

As described earlier, the CrIS/ATMS instrument suite forms a single sounding system (CrIMSS). However, the CrIMSS retrieval approach is based on the assumption that the CrIS and ATMS instruments are viewing the same air mass and the same surface "footprint" at the same time. The details of the required alignment and synchronization are beyond the scope of this document. Here, we will simply point out that there are differences between the operational aspects of CrIS and those of ATMS that present challenges to achieving this goal. For example, CrIS completes a single scan cycle in 8 seconds, with 30 samples of a 3x3 cluster of individual FOVs and each cluster separated by 3.33°. While the resulting spatial sampling density is nearly identical to that of ATMS, their scan speeds differ markedly (i.e., three vs. one scan cycle every 8 seconds), which causes significant alongtrack misalignment at the scan swath edges. Alignment could be optimized (but not made perfect, due to the fact that the CrIS 3x3 sample cluster rotates with scan angle in a manner similar to that of the ATMS polarization vectors) by mounting CrIS with a slight (less than 1°) positive yaw angle relative to ATMS or by mounting ATMS with a negative yaw relative to CrIS. Synchronization is more easily achieved, by introducing a time offset between the occurrence of the 8-second sync pulse and the start of a new scan cycle (which is defined as the start of the first Earth sample interval). ATMS has been designed to allow for such a delay, with a value that can be commanded from the ground. The objective of co-alignment and synchronization is usually to achieve close spatial coincidence between the respective "footprint" patterns projected on the ground. The AIRS-AMSU system incorporates both a yaw correction and synchronization, but the HIRS-AMSU system does not incorporate a yaw correction nor synchronization. Instead, HIRS-AMSU data is spatially interpolated, to achieve a synthesized alignment. Since such an approach is vulnerable to processing artifacts, physical alignment and synchronization is a preferred method whenever possible. The CrIS-ATMS system relies on a Backus-Gilbert algorithm (Backus and Gilbert, 1970) to generate ATMS footprints that match the CrIS footprints in both size and location. A study has shown that with a proper footprint-matching algorithm, the difference with and without having a mechanical alignment is small (Blackwell and Chen, 2005).
.

5. In-flight Calibration System

As described in Section 3 (Instrument description), and illustrated in Fig. 6 (scan sequence), each of the two ATMS antenna/receiver systems measures the radiation from two calibration sources during every scan cycle. The first source is the cosmic background radiation emanating from space. This source is viewed immediately after the earth has been scanned. The antenna is quickly moved to point in a direction between the earth's limb and the spacecraft's horizon. There it drifts slowly while four cold space measurements are taken. The second source is an internal blackbody calibration target (often called a "warm load"), which is at the ambient internal instrument temperature. After the space calibration view the antenna is quickly moved to point in the zenith direction, where the blackbody target is located. Again, the antenna drifts slowly while warm target measurements are taken. Thus, two sets of cold and warm calibration measurements that bracket the earth scene measurements are obtained for every scan cycle. A full discussion of calibration issues can be found in a document produced by NGES[1].

Such a through-the-antenna calibration system allows most of the system losses and instrument defects be calibrated, since the calibration measurements involve the same optical and electrical signal paths as earth scene measurements. The only exception is that the internal calibration target appears in the antenna near field and can reflect leakage emission from the antenna itself. However, this effect is taken into account with the so-called bias corrections in the calibration processing. The through-the-antenna calibration system has an advantage over a calibration system that uses switched internal noise sources injected into the signal path outside the antenna to achieve some weight gain since the internal calibration target is fairly massive.

The purpose of the calibration measurements is to accurately determine the so-called radiometer transfer function, which relates the measured digitized output (i.e., the counts C) to the associated radiometric "brightness" temperature:

$$T_\text{B} = F(C) \tag{1}$$

This function, which is illustrated schematically in Fig. 7 in which the subscripts c and w refer to the cold and warm calibration points, respectively, and the subscript s refers to an Earth scene, depends primarily on channel frequency and instrument temperature. The radiometer transfer function could also undergo short term and long term changes due to gain fluctuations and drift due to aging and other effects. Note that others, notably NOAA, use the physical quantity called radiance, which has unit of mW/m^2-sr-cm^{-1}, instead of the brightness temperature that ATMS calibration uses here, which has unit of K. It is a simple matter to convert radiance to brightness
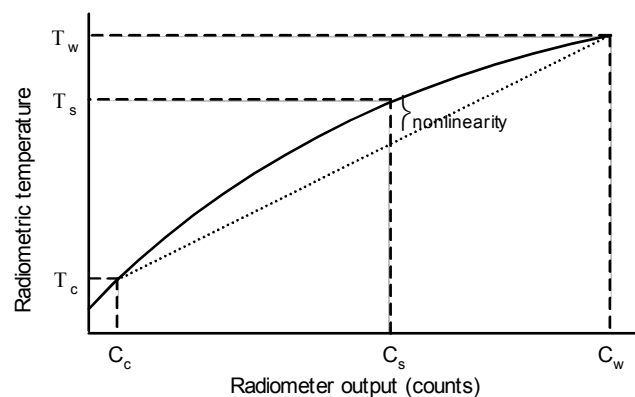
Figure 7. Transfer function schematically

---

[1] "ATMS Radiometric Math Model", NGES Report 12110C (October 2005)

temperature and vice versa. However, the Rayleigh-Jeans approximation from converting radiance to brightness temperature is valid under the condition that $(C_2\upsilon)/T \square\ 1$, where υ is the wavenumber. At colder temperatures or shorter wavelengths, this approximation results in significant biases that need to be quantified and corrected (Weng and Zou, 2013).

If the transfer function were perfectly linear, then any two calibration points could be used to uniquely determine its form (i.e., the two linear coefficients, a_0 and a_1) at the time of the calibration measurements:

$$F_{\text{lin}}(C) = a_0 + a_1 C \qquad (2)$$

While it has been a goal (and a requirement) in radiometer instrument design to make the transfer function as linear as possible, it is slightly nonlinear in reality. To account for the slight nonlinearity a quadratic term (i.e., $a_2 C^2$) is added to Eq. 2:

$$F_{\text{nonlin}}(C) = a_0 + a_1 C + a_2 C^2 \triangleq F_{\text{lin}}(C) + Q(C) \qquad (3)$$

Being zero at the two calibration points (e.g., C_c and C_w), the quadratic term (i.e., nonlinearity) can be uniquely expressed as follows

$$Q = 4x(1-x)T_{\text{NL}} \qquad (4)$$

where x is a measure of the relative distance of an Earth scene point from the two calibration points,

$$x = (T_s - T_c)/(T_w - T_c) \qquad (5)$$

and T_{NL} is the peak nonlinearity, occurring at the midway point, i.e., at $x = 0.5$, for a given channel (Weng et al., 2013). Once the magnitude of T_{NL} is determined, the nonlinearity term, Q at every temperature point between the two calibration points can be computed via Eq. 4.

It is emphasized that these expressions pertain to a quadratic nonlinearity model, which is a good approximation since the nonlinearities are generally quite small. It is also noted that determining T_{NL} from ground measurements is not straightforward, and detecting changes in its value after the launch of satellite (a distinct possibility) is even more difficult. In principle, this parameter may be a function of instrument temperature and other variables. The current algorithm allows a choice of using a fixed set of nonlinearity values or determining them from a function of the instrument temperature and the redundancy configuration. The receiver shelf temperature (K/KA Shelf, V Shelf, W Shelf, and G Shelf) is used to interpolate between tabulated pairs obtained from pre-launch thermal vacuum test data. Each tabulated pair consists of a receiver temperature and a nonlinearity term.

Equation (3) was used for AMSU by both NOAA and NASA. The calibration algorithm describes how to compute the linear and quadratic coefficients. The approach proposed for ATMS is to first use the linear approximation (equivalent to equation (2)) and then to make a quadratic correction using equation (4). The linear approximation is simply a representation of a straight line through the two calibration points (the dotted line in Fig. 7):

$$T_{\text{B,lin}} = T_{\text{w}} + [(T_{\text{w}} - T_{\text{c}})/(C_{\text{w}} - C_{\text{c}})](C_{\text{s}} - C_{\text{w}}) \tag{6}$$

i.e., the linear coefficients are

$$a_1 = (T_{\text{w}} - T_{\text{c}})/(C_{\text{w}} - C_{\text{c}}) \tag{7}$$

$$a_0 = T_{\text{w}} - a_1 C_{\text{w}} \tag{8}$$

The inverse of a_1 is often called the "gain", which is an important measure of radiometer output for a given instrument temperature:

$$g = 1/a_1 = (C_{\text{w}} - C_{\text{c}})/(T_{\text{w}} - T_{\text{c}}) \tag{9}$$

The following subsections sequentially discuss how the warm and cold calibration points are obtained, and the sources of the measurement errors and uncertainties. Discussion of how to determine the Earth scene brightness temperatures is also given in the subsequent section.

5.1 Blackbody View

The internal calibration targets are approximately cylindrical in outline and are made up of pyramid shaped metal structures coated with an absorbing material. Figure 8 shows an AMSU calibration target, which is very similar to the ATMS targets. For the larger aperture, the pyramids are about 1 cm across and about 4 cm high. The use of metal for the base and core ensures that temperature gradients across the targets are minimal, while the pyramid structure and the absorbing coating ensure that the emissivity is close to 1. The target is surrounded by a metal shroud that mates very well with a matching shroud surrounding the rotating reflector antenna in order to prevent the stray radiation from external sources to affect the warm calibration measurements. For ATMS whose antenna moves during calibration

Figure 8. Typical warm load

measurements, the calibration target is slightly larger than the antenna shroud aperture, so that the antenna has a full view of the target during the entire calibration period.

n order to reduce the effect of random noise, the calibration target is consecutively viewed four times. (Consecutive samplings are used in lieu of a single sampling of longer duration in order to keep the data collection control system simple.) The effective calibration measurement noise, after averaging, is then reduced by a factor of two below the NEΔT values listed in Table 1. These values can be further reduced by averaging over several calibration cycles, as will be described later. The four consecutive measurements are assumed to be entirely equivalent, which remains to be tested both on the ground and on-orbit. The calibration algorithms may have to be modified if this assumption turns out to be faulty.

The emissivity of the calibration targets is required to be at least 0.9999. This is necessary in order to keep radiation that is unavoidably emitted from the radiometer's local oscillators through the antenna and reflected back from the calibration target to a minimum. For example, such radiation could masquerade as a radiated brightness temperature of as much as 100 K. An emissivity of 0.9999, and thus a reflectivity of 0.0001, would then yield a reflected contribution of 0.01 K – a negligible amount. In reality, the measured ATMS target emissivities exceed 0.9999, and the maximum emission from the antenna has been measured to be less than 100 K using a "tunable short test".

The targets are not thermally controlled. Being insulated from external thermal swings (and the entire instrument is thermally insulated from the platform), the target temperatures will not change rapidly (less than 0.001 °C/sec) and that temperature gradients across the targets will be small (less than ±0.05 °C). To ensure good knowledge of the target temperatures, there are eight and seven temperature sensors (Platinum Resistance Thermometers - PRTs) embedded throughout the KAV and WG targets, respectively. Measurement accuracy is better than 0.1°C. The PRTs are embedded in the metal structure from the back and are close to the coated front surface.

The vertical temperature gradient in the pyramid structure is not measured but difficult to model and predict, Radiation at the shorter wavelengths may originate from a particular part of the pyramids while longer wavelengths may originate from a different area – e.g., tips vs. troughs. There are indications from previous studies that such gradients can influence calibration accuracy. Temperature gradients in a periodic structure as in the ATMS targets can also cause resonant effects such as grating "sidelobes". The on-orbit performance may therefore be somewhat poorer than measured on the ground where benign and controlled conditions are usually maintained. Bias corrections determined from the thermal vacuum tests on the ground may compensate for some of these effects, however.

In general, there could be a small difference between the brightness temperature computed from the physical temperature of the target and the estimated emissivity and the brightness temperature inferred from the radiometer output, which can be caused by effects such as discussed above. One of the objectives of the ground based thermal-vacuum measurements, where operational conditions are simulated as closely as possible, is to determine the magnitude and biases of such differences. It is accomplished by observing a NIST-traceable reference target in lieu of an Earth "scene". Since the brightness temperature of such a target is known with better accuracy than that of the ATMS internal warm loads, it is possible to use it to infer the warm load biases. Although quite small, the warm load biases may be of the same magnitude as the target calibration accuracy and must therefore be accounted for in the calibration processing. The warm load biases may depend on the physical temperature of the receiver system.

5.2 Cold Space View

There are four cold space calibration beam groups located at 6.66°, 8.33°, 10.00°, and 13.33° below the anti-sun normal toward nadir in the scan plane. Which beam group to use is selected by ground command. Within a beam group, the cosmic background radiation is sampled four times consecutively, with two neighboring samples being spaced 1.11° apart. However, the radiative environment for the cold space view is much more complicated than for the warm calibration target view. Although the cosmic radiometric temperature is well-known (e.g., 2.726

± 0.004 K), significant radiation from the earth as well as earth radiation reflected from spacecraft structures can enter the radiometer receiver through the antenna sidelobes. Figure 9 provides a conceptual illustration. For example, we can estimate an uncertainty on the order of 0.1-0.2 % of what is received from the 124° sector that "sees" Earth from an 828 km orbital altitude of JPSS (The orbital altitude for Suomi NPP is 824 km). This contribution corresponds to 0.25-0.5 K, which is about 1/10 to 1/5 of the cosmic radiation. This is not insignificant. But the impact on calibration accuracy is relatively small, which is discussed in the next section. Contributions due to reflections from the structures and surfaces on the spacecraft are probably minor. Radiation emitted from the spacecraft is expected to be negligible, since most surfaces will be covered with MLI blanket − a metallized Mylar material that is highly reflective at microwave frequencies.
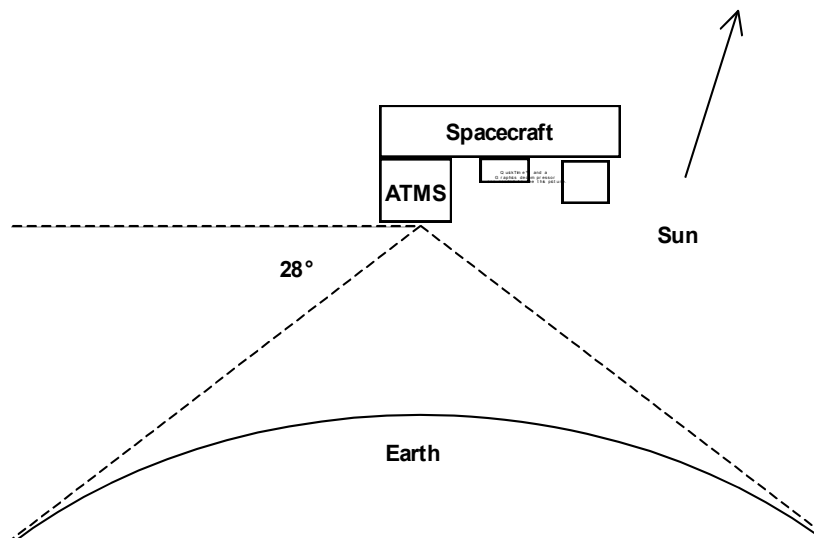
Figure 9. Space view geometry
(flight direction is toward the reader, out of the page)

Figure 9 also suggests that the Earth sidelobe radiation probably depends on the exact pointing direction and is likely to be greatest when the antenna boresight is closest to the Earth. This means that, for a given nominal space calibration position, the sidelobe contribution may vary between the four consecutive samples, which cover an angular range in excess of 4°. The baseline algorithm averages these together to reduce the effective noise. An additional analysis shall be undertaken to determine an on-orbit correction.

Instead of radiance, the Rayleigh-Jeans approximation for brightness temperature is used for ATMS SDR calibration algorithm. Under the Rayleigh-Jeans approximation and ignoring the emissivity, the radiance is linearly proportional to the physical temperature:

$$B \approx CT \qquad (10)$$

The Rayleigh-Jeans approximation is valid for a low-frequency, high-temperature situation, but breaks down for high frequency and low temperature situations (Weng and Zou, 2013). which is the case for the low brightness temperatures normally encountered during the cold calibration. To correct for the error resulting from the Rayleigh-Jeans approximation, the cold calibration brightness temperature inputs to the SDR processing algorithm are adjusted (see section 5.3 in the "ATMS Radiometric Math Model" referenced earlier).

Finally, one should note that the cold space view could also be contaminated by a lunar intrusion. From time to time (i.e., on a quarterly cycle), the Moon is near half-full when seen from the spacecraft. The Moon light may approach the field of view of one or more of the space view positions. In the worst case when the Moon is exactly in the boresight direction, the Moon light can elevate the space view brightness temperature by up to 30 K for the channels with a 1.1° FOV, up to 5 K for the channels with a 2.2° FOV and 1 K for the channels with a 5.2° FOV. The Moon effect may be detectable for a period up to 40 minutes. When this happens, it is necessary to either account for the increase in space view brightness temperature (i.e., model it) or reject the observation from calibration processing based on prediction or detection. Details of the lunar intrusion correction are given in the next section.

5.3 Sources of Errors and Uncertainties

This section summarizes the sources of errors and uncertainties in the calibration process. A detailed analysis can be found in the NGES "Radiometric Math Model" report referenced earlier.

Errors can be classified as bias errors and random errors. The bias errors are static and independent, and thus can be combined by direct addition. The random errors are uncertainties due to random fluctuations of the instrument characteristics. They are assumed to be independent, and can be added up in a root-sum-squared (RSS) sense. (This is not strictly correct, but the resulting errors in the uncertainty estimates are judged to be relatively small.) Theoretically speaking, all known biases can be removed by calibration, so that only the uncertainties remain.

As was explained at the beginning of this section, the on-orbit calibration procedure consists of determining the linear part of the transfer function at two calibration points, the cold space calibration view and the internal blackbody calibration view, as well as the quadratic function between the two anchor points. The peak amplitude of the quadratic deviation from linearity, denoted by T_{NL} in equation (4) is assumed to be a fixed value for each channel, and possibly a function of the instrument temperature. The transfer function thus determined is then used to convert earth scene radiometer measurements to corresponding brightness temperatures. The absolute accuracy of this scene brightness temperature is termed the calibration accuracy. The *calibration accuracy* is strictly defined as the mean difference between the inferred and the actual brightness temperature. It can be expressed as

$$\Delta T_{\mathrm{B}} = \mathrm{RSS}\{x\Delta T_{\mathrm{w}};\ (1-x)\Delta T_{\mathrm{c}};\ 4x(1-x)\Delta T_{\mathrm{NL}};\ \Delta T_{\mathrm{sys}}\} \tag{11}$$

where "RSS" means that the result is the square root of the sum of the squares of the terms. The factor x is defined in Eq. 5, and $\Delta T_{\mathrm{w}}, \Delta T_{\mathrm{c}}$ and ΔT_{NL} are the respective uncertainties in the calibration radiometric temperatures and the nonlinearity amplitude. ΔT_{sys} is an uncertainty due to random instrument fluctuations (e.g., gain fluctuations). Note that Eq. 11 expresses the uncertainty only and no biases are included in it.

Although scene temperatures may be as low as 80-90 K at the high frequencies, the meaningful operational dynamic range is 200-300 K for sounding channels and about 140-300 K for window channels. Substantially lower sounding temperatures are caused by scattering from raindrops or ice above precipitating cells, which are conditions that currently cause the retrieval process to

fail. (It is possible that scattering may be included in the retrieval algorithms in the future, however.) Very transparent window channels, where a low ocean emissivity makes ocean scenes appear very cold radiometrically, are also not crucial to the retrieval processing. Thus, the effective meaningful dynamic range is 200-300 K. With a T_w on the order of 300 K and T_c close to zero, the meaningful dynamic range for x is 2/3 to 1. In the worst case ($x{\sim}2/3$) the relative weights of the first two terms in Eq. 11 are then 4/9 and 1/9, respectively. This means that if $\Delta T_w = \Delta T_c$, errors in T_c contribute four times less to the overall calibration accuracy than errors in T_w, and are considerably less than that for most scenes. It is useful to keep this perspective in mind when the error sources are discussed.

In the following the sources contribute to the above uncertainties are briefly discussed. Interested readers are referred to the NGES Radiometric Math Model document for a thorough and detailed discussion.

Blackbody error sources
This error stems from *uncertainty* in the knowledge of the following four factors:
a) blackbody emissivity,
b) blackbody physical temperature,
c) reflector/shroud coupling losses, and
d) reflected local-oscillator leakage.
Of these, the second term is expected to dominate.

The *emissivity* is generally known to be in a range of [ε_{min}, 1.0]. A typical value for ε_{min} is 0.99993. Due to limited measurement accuracy, the emissivity should be interpreted as

$$\varepsilon = 1.0 - (1.0 - \varepsilon_{min})/2 \pm \Delta\varepsilon \tag{12}$$

where $\Delta\varepsilon$ is the estimated uncertainty. It is bounded by $(1.0 - \varepsilon_{min})/2$. For the example quoted, where ε_{min} is estimated to be 0.99993, an uncertainty of less than 0.000035 would be estimated. An alternative estimate could be based on an analysis of the measurements of the reflectivity that can be used to determine the emissivity.

The *blackbody physical temperature* uncertainty can be caused by the following four factors
a) surface temperature drifts between the time of temperature measurement and the time of radiometer measurement (ΔT_{drift}),
b) temperature gradients in the blackbody (ΔT_{grad}),
c) temperature measurement uncertainties (ΔT_{meas}), and
d) vertical gradients and uncertain origin of the radiation (ΔT_{vert}).
The last factor is currently unknown, but could dominate the blackbody physical temperature uncertainty

The *reflector/shroud coupling losses* occur because the antenna and blackbody shrouds do not mate perfectly, and external radiation (from the interior of the instrument) will enter the antenna through the gap between the shrouds. This effect is uncertain because of uncertainties in measuring and modeling the coupling losses as well as uncertainties in the knowledge of the external radiation. The magnitude of this is expected to be very small and can be ignored.

Finally, the *leakage* signal originating from the local oscillators (LOs) and emitted by the antenna may be reflected back to the antenna, if its emissivity is not unity (i.e., if its reflectivity

is not zero). This is uncertain because both the leakage signal and the target reflectivity (or emissivity) are not precisely known. The latter is expected to dominate, and the former can be ignored. The reflected LO signal may also interfere with itself by changing the operating point of the detector system, which then impacts the intrinsic noise level of the amplifier. Thus, although the LO interference may be well outside the IF passband and therefore not directly measurable, it can still significantly impact the apparent output noise of the system.

The resulting uncertainty is

$$\Delta T_{\mathrm{w}} = \mathrm{RSS}\{\Delta \varepsilon T_{\mathrm{w}}; \ \Delta T_{\mathrm{drift}}; \ \Delta T_{\mathrm{grad}}; \ \Delta T_{\mathrm{meas}}; \ \Delta T_{\mathrm{vert}}; \ \Delta \varepsilon T_{\mathrm{LO}}\} \tag{13}$$

where T_{LO} is the leakage radiance, expressed as a brightness temperature.

Only the first term is expected to change on orbit, so this can be contracted to

$$\Delta T_w = \left\{ [\Delta \varepsilon T_w]^2 + \left[\Delta T_{w,fixed}\right]^2 \right\}^{1/2} \tag{14}$$

where $\Delta T_{w,fixed}$ represents the unchanging terms compiled from ground measurements.

Cold calibration (space view) error sources
This error stems from uncertain knowledge of the following three factors:
a) Earth contamination through the antenna sidelobes,
b) spacecraft contamination through the antenna sidelobes, and
c) the cosmic background temperature.

The *sidelobe contamination* is uncertain due to uncertain knowledge of the antenna pattern (i.e., sidelobes) as well as uncertain knowledge of the radiation from Earth and the spacecraft. The latter consists mostly of reflected Earth radiation, since most visible surfaces will be covered by reflective materials, as discussed above. Both effects may be modeled and pre-computed, but the associated uncertainties are expected to be substantial. This is the largest contribution to this term.

We may express the sidelobe radiation as the product of an effective antenna efficiency, a_{eff}, which is defined over the sector that receives this radiation, and an effective scene temperature for that sector, T_{eff}:

$$T_{\mathrm{SL}} = a_{\mathrm{eff}} T_{\mathrm{eff}} \tag{15}$$

The uncertainty is then the first-order variation of T_{SL}:,

$$\Delta T_{\mathrm{SL}} = \mathrm{RSS}\{\Delta a_{\mathrm{eff}} T_{\mathrm{eff}}; \ a_{\mathrm{eff}} \Delta T_{\mathrm{eff}}\} \tag{16}$$

The uncertainty in a_{eff}, is primarily due to uncertain antenna patterns (from which it is usually computed), and the uncertainty in T_{eff} is primarily due to an uncertain or variable mean brightness temperature of the visible Earth disc. There is also an error component caused by representing the sidelobe radiation as the simple product shown in Eq. 15. In reality the right-hand-side of equation (15) involves a double integral, i.e., a convolution between the two variables. It may be noted that the effective scene temperature varies along the orbit. There are latitudinal (i.e., intra-orbital), longitudinal (i.e., inter-orbital) and temporal (e.g., inter-seasonal) variations in the effective brightness temperature of the visible portion of the Earth. This may be

modeled or estimated in other ways, or it may be ignored instead of being carried as an additional uncertainty.

Finally, although the *cosmic background temperature* is well known, there is an uncertainty associated with it. However, it can be ignored here, since the uncertainty of the sidelobe radiation is expected to dominate the cold calibration uncertainty. The result is

$$\Delta T_{\mathrm{c}} \approx \Delta T_{\mathrm{SL}} = \mathrm{RSS}\{\Delta a_{\mathrm{eff}} T_{\mathrm{eff}}; \; a_{\mathrm{eff}} \Delta T_{\mathrm{eff}}\} \tag{17}$$

Instrument (transfer function) error sources
This error stems from uncertainty in the knowledge of the following four factors:
a) nonlinearities,
b) system noise,
c) system gain drift, and
d) bandpass shape changes.

The *nonlinearities* can be modeled as a quadratic term that may be a function of a characteristic instrument temperature, as discussed above. This is only an approximation and is therefore uncertain. In addition, as for the blackbody, the instrument temperature is not known precisely. However, the latter effect is ignored. The former is expressed in terms of the uncertainty of the peak nonlinearity, ΔT_{NL} in Eq. 11.

The system terms are due to random fluctuations and are characterized in terms of standard deviations. They are channel dependent, as are most of the effects discussed above. The combined effect is expressed as T_{sys} in Eq. 11.

6. Calibration Processing Steps

In this section we describe how the on-board calibration measurements are used to determine the calibration coefficients, as discussed in Section 5. In summary, the procedure – illustrated in Fig. 10 – is as follows. Each channel is treated separately.

- Determine the blackbody brightness temperature, T_w from its physical temperature as measured by the embedded PRTs with a possible temperature dependent bias correction
- Estimate the cold-space brightness temperature, T_c, by taking into account of the earth radiation into the antenna sidelobes and a correction to the Rayleigh-Jeans approximation
- Average the blackbody and cold-space radiometer counts, C_w and C_c, measured in a calibration cycle (i.e., up to 4 values) and smooth the averages over several calibration cycles
- Determine the radiometer gain, from Eq. 9
- Estimate a scene brightness temperature from the linear approximation of Eq. 6
- Use the linear approximation to estimate the relative brightness temperature, x in Eq. 5
- Estimate the radiometer peak nonlinearity amplitude, T_{NL}, in Eq. 4, based on the measured instrument (shelf) temperature
- Compute the quadratic correction of the brightness temperature based on Eq. 4
- This implicit transfer function is applied to the earth-scene radiometer counts for each scan cycle.
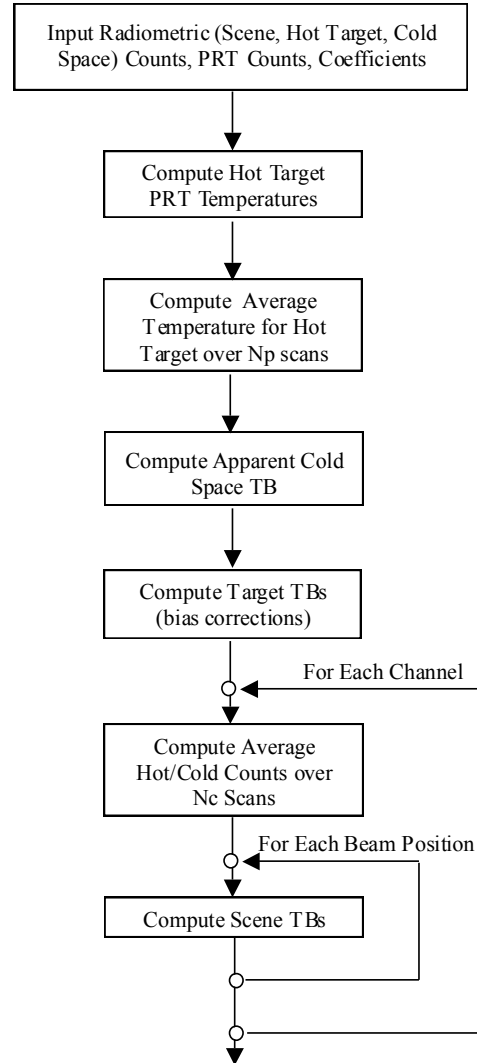
Figure 10. Calibration flow chart

6.1 Physical Temperatures

Several calibration steps require the conversion of a PRT raw count to a corresponding physical temperature. The procedure for such conversions is common to all PRTs. In essence, a PRT is a passive sensor with a resistance that is a known function of temperature. An analog-to-digital

converter (ADC) outputs a digital 'count' that is proportional to the resistance, which is inserted into the telemetry. The conversion to temperature on the ground consists of two steps. In the first step, the resistance is reconstructed with a linear transfer function that is calibrated with on-board measurements of a known reference resistor (the so-called precision analog monitor – PAM). This conversion is

$$R_{\mathrm{PRT}} = R_{\mathrm{PAM}}\,(C_{\mathrm{PRT}} - C_{\mathrm{off}})/(C_{\mathrm{PAM}} - C_{\mathrm{off}}) \qquad (18)$$

where C_{off} refers to a reference count with shorted inputs (i.e., zero resistance). Thus, the essentially linear ADC is "calibrated" on-board with two reference measurements, just as is done for the slightly nonlinear radiometer.

The second step is to convert the resistance to a temperature value. Here, the transfer function – called the Callendar-Van Dusen equation – is nonlinear:

$$R_{\mathrm{x}} = R_0\{1 + \alpha[T_{\mathrm{x}} - \delta(T_{\mathrm{x}}/100 - 1)(T_{\mathrm{x}}/100) - \beta(T_{\mathrm{x}}/100 - 1)(T_{\mathrm{x}}/100)^3]\} \qquad (19)$$

where R_0, α, β and δ are characteristic coefficients and are determined by the manufacturer for each individual PRT. The temperature T_{x} iin Eq. 19 is in unit °C. This equation is solved for T_{x} by the Newton-Raphson iteration. A simpler but less robust alternative approach, used with the AMSU systems, is to fit a cubic polynomial, $T = c_0 + c_1 C + c_2 C^2 + c_3 C^3$, to the two functions expressed in Eqs. 18 and 19.

Using this method, all PRT readings are converted to temperatures.

6.2 Effective Blackbody Brightness Temperature

Physical temperature
In summary: The warm load physical temperature is determined as the average value derived from the embedded PRTs readings plus a bias-like correction factor, which is allowed to depend on the receiver's physical temperature. A weighted average in two dimensions (PRT # and across-scan sample) is implemented that allows for a weighted average. This makes it possible
a. to give more weight to certain PRTs than others, and
b. to implement a variable, time-dependent weighting coefficients (i.e., samples closest in time are given larger weightd than those further away)

The weighting coefficients are specified in ancillary processing tables that can be changed if necessary.

The result is an effective warm load physical temperature, T_{w}.

Bias correction
The warm load bias correction may be applied in two ways. The first option applies a fixed bias for each of the five bands (K, Ka, V, W and G). The K band covers channel 1. The Ka band covers channel 2. The V band covers channels 3-15. The W band covers channel 16. The G band covers channels 17-22. For the second option, a temperature dependent bias correction, which is assumed to be a quadratic form, is applied for each channel

$$\Delta T_{\mathrm{w}} = a + bT_{\mathrm{BP}} + cT_{\mathrm{BP}}^2 \qquad (20)$$

where the coefficients a, b and c are also specified in the ancillary data tables. One set for each channel. T_{BP} is an instrument temperature representative of the receiver base plate. It is thus possible to allow for any slightly nonlinear temperature dependent biases to be determined from ground testing. Extensive analysis of test data is required for this implementation (e.g., identification of temperature dependence using polynomial functional fits).

Warm load brightness temperature
The warm load brightness temperature is now calculated as

$$T_{\mathrm{w}} = T_{\mathrm{w}} + \Delta T_{\mathrm{w}} \qquad (21)$$

6.3 Effective Space Brightness Temperature

Cosmic background temperature
A value of 2.728 K is used for the cosmic background temperature, T_{c}.

Rayleigh-Jeans correction
A correction has been pre-computed that accounts for deviations from the Rayleigh-Jeans approximation at the low space brightness temperatures.

Sidelobe bias correction
As discussed above, there may be substantial radiation received from the relatively warm Earth through the antenna sidelobes while the antenna is pointing at space. A set of correction values (ΔT_{SL} and one for each channel) has been computed from the measured antenna patterns and a simple climatological model of the Earth. (This does not account for the fact that the actual mean scene temperature varies, as was discussed above.) The current implementation allows two choices, either using one value for each of the five bands (K, Ka, V, W and G) or one value for each of the 22 channels.

Space view brightness temperature

The cold calibration brightness temperature is now calculated as

$$T_{\mathrm{c}} = \left(2.728 + \Delta T_{\mathrm{RJ}}\right) + \Delta T_{\mathrm{SL}} \qquad (22)$$

where the values within the parentheses are pre-computed, stored in ancillary tables and simply read from those tables.

Lunar contamination

As mentioned above, it is likely that the Moon light will enter the cold-calibration FOV from time to time and contaminate the apparent space brightness temperature. The cold space view temperature increase caused by the lunar contamination is estimated[2] as:

---

[2] Seiichiro Kigawa and Tsan Mo: "An Algorithm for Correction of Lunar Contamination in AMSU-A Data", NOAA Technical Report NESDIS 111 (Dec 2002)

$$\Delta T_{\mathrm{c}} = \exp\left[-\frac{(\alpha-\alpha_0)^2}{2\alpha_s^2}\right] \exp\left[-\frac{(\delta-\delta_0)^2}{2\delta_s^2}\right] \times \beta \times T_{\mathrm{moon}} \times \left(\frac{60.3\times6278}{d}\right)^2 \tag{23}$$

where α : lunar azimuth [degrees]
    α_0 : FOV center azimuth [degrees]
    α_s : FOV azimuth size factor [degrees]
    δ : lunar elevation [degrees]
    δ_0 : FOV center elevation [degrees]
    δ_s : FOV elevation size factor [degrees]
    β : nominal area ration of moon to FOV
    d : distance between satellite and moon [km]
    T_{moon} : effective moon temperature [K]
        $= 95.21 + 104.63(1-\cos\theta) + 11.62(1+\cos 2\theta)$
   θ: separation angle between moon and sun (θ=180° in case of Full Moon)

Eq. 23 may be simplified if the following approximations are made:
(a) assuming that the antenna patterns are circularly symmetric,
(b) ignoring the FOV center offsets, and
(c) ignoring the satellite to moon distance variation correction.

Eq. 23 is then reduced to:

$$\Delta T_{\mathrm{c}} = \exp\left[-\frac{\gamma^2}{2\gamma_s^2}\right] \times \beta \times T_{\mathrm{moon}} \tag{24}$$

where γ : angle between the cold space view and the moon [degrees]

    $\gamma_s = \frac{\gamma_{3dB}}{2.35}$, where γ_{3dB} is the 3dB beamwidth [degrees]
    $\beta = \frac{1}{2}\left(\frac{r_{moon}}{\gamma_s}\right)^2$, where radius of the moon: $r_{moon} = 0.255$ deg

For each of four cold space view readings, if ΔT_{c} is larger than a threshold of 0.2 K, this cold space view reading is flagged as being contaminated by lunar intrusion and excluded in the SDR calibration. It needs to be pointed out that ΔT_{c} is only used for detecting the contaminated cold space view reading, not used to correct it.

If not all of four cold space view readings are contaminated by lunar intrusion, those uncontaminated readings (e.g., up to four readings) are used in the calibration processing. However, there is high possibility that all four readings are contaminated in a single scan line, particularly for the channels with a 5.2° FOV. To avoid data gap (could be up to 200 scans), cold space view readings have to be corrected or replaced in order to produce reasonable brightness temperatures. Instead of applying the previous method, which uses some pre-filled cold space view values for correction, the current operational system uses the most recent uncontaminated cold space view readings to replace the contaminated readings in the all four-reading contaminated case due to its effectiveness and simplicity. However, the closest uncontaminated scan could be a few hundred scan lines apart in some extreme cases, in which these so-called "closest and correct" cold space view readings might not be very representative due to the drift of radiometer gain.

6.4 Radiometric Calibration Counts

Each of the two calibration targets (i.e., the warm load and cold space) is sampled four times in succession. The measurements are in the unit of digital "counts", which represent the radiometer's output. It is assumed that the radiative environment does not change between successive samplings, so that any differences between the measurements are strictly due to noise, which can be reduced by averaging or smoothing the measurements. However, as discussed above, this assumption must be tested on-orbit and may not be valid. Should that be the case, the present calibration algorithms need to be modified accordingly.

The procedure implemented is simply to compute a count averaged over the four in-scan samples and over several scans. Ancillary tables are used to specify the respective weights. There are two types of weighting functions that are used, including triangular and boxcar functions (Weng et al., 2013). From Suomi NPP ATMS on-orbit data, it is found that there is a striping noise (1/f flicker noise) in along-track direction. In the operational processing system, the boxcar function is used for computing the mean warm and cold calibration counts in the two-point calibration since it is more effective in reducing the striping noise. The averaging interval in the time domain (e.g. number of scan lines) is determined from a power spectrum analysis of the warm and cold counts which determine the location of 1/f "knee". However, since the 1/f flicker noise is also present in the earth scene count, an averaging of warm or cold counts alone cannot completely eliminate the striping in brightness temperatures, especially for WG bands. It is found that the striping noise for KAV bands is generally on an order of 0.25K but the magnitudes at WG bands can be as much as 1.0K after the boxcar function is applied for warm and cold count averaging.

6.5 Earth Scene Brightness Temperatures

First the gain g is computed by Eq. 9. This allows for a linear estimate of the brightness temperature, $T_{B,lin}$ to be determined, which in turn enables the computation of a corresponding x-factor by Eq. 5, denoted as x_{lin}. Finally, Eq. 4 is used to compute a nonlinear correction term, assuming that. The sequence is listed below:

$$g = (C_w - C_c)/(T_w - T_c) \tag{25}$$

$$T_{B,lin} = T_w + (C_s - C_w)/g \tag{26}$$

$$x_{lin} = (T_{B,lin} - T_c)/(T_w - T_c) \tag{27}$$

$$Q = 4x_{lin}(1 - x_{lin})T_{NL} \tag{28}$$

$$T_B = T_{B,lin} + Q \tag{29}$$

This is done for each channel at each scan position.

6.6 Data Quality Control

The SDR code examined for the first version of this document contains only rudimentary data quality control (QC) and quality assessment (QA). Subsequent algorithm updates have incorporated additional quality checking process.

PRT Quality Checks:

1) PRT quality check – limits

The converted warm load PRT temperatures are checked against predetermined gross limits. Those falling outside the limits are considered "bad":

$$T_i < T_{low} \text{ or } T_i > T_{upp} \rightarrow \text{"bad-}T_i\text{"}$$

2) PRT quality check – self-consistency

The PRT temperatures are then checked for self-consistency (i.e., data fluctuation). This is done by comparing all temperatures not flagged as bad with each other. Any PRT's temperature that differs by more than a fixed limit from at least two other PRTs readings will be flagged as "bad":

$$|T_i - T_j| > \Delta T_{max} \text{ and } |T_i - T_n| > \Delta T_{max} \rightarrow \text{"bad-}T_i\text{"}$$

The number of "good" PRTs is then checked. If there are less than 5 "good" PRTs for the KAV target or 4 for the WG target, all PRTs within that group will be flagged as "bad". These numbers can be adjusted in the ancillary parameter file. "Bad" PRTs are excluded from the calibration process.

3) PRT quality check – data sufficiency

If the weight-sum of "good" PRT readings used in the multi-scans averaging falls below a specified percentage, it is deemed not possible to reliably determine the warm load temperature for the current calibration cycle:

$$(\textstyle\sum_i W_i)/W_{total} < W_{threshold\_prt} \rightarrow \text{"bad-}\overline{T}_W\text{"}$$

Failing the data sufficiency test will result in an unsuccessful calibration cycle.

Warm Count Quality Checks:

1)   Quality check – limits

Each count from each channel is checked against pre-defined channel-specific gross limits. Those fall outside the limits are flagged as "bad":

$$Cw_i < Cw_{low} \text{ or } Cw_i > Cw_{upp} \rightarrow \text{"bad-Cwi"}$$

2)   Quality check – self consistency

The counts are checked for self-consistency. Each count not flagged as "bad" is compared with other counts in the same scan. Any count that differs by more than a fixed limit from at least two other counts will be flagged as "bad":

$$|Cw_i - Cw_j| > \Delta Cw_{max} \text{ and } |Cw_i - Cw_k| > \Delta Cw_{max} \rightarrow \text{"bad-Cw}_i\text{"}$$

The number of "good" samples is then checked. If there are less than three "good" samples, this scan will be flagged as "bad" and not included in the multi-scans averaging.

3)   Quality check – gain error

If the lowest "good" warm count is smaller than or equal to the highest "good" cold count, all the warm counts and cold counts from this scan will be flagged as "bad" and not included in the multi-scans averaging.

4)   Quality check – data sufficiency

If the weight-sum of all "good" scans falls below a specified percentage, it is deemed impossible to reliably determine the averaged warm count for the current calibration cycle. Failing the data sufficiency test will result in an unsuccessful calibration cycle.

Cold Count Quality Checks:

The cold count quality checks are identical to the warm count checks, with limits appropriate for the cold counts.

All the limits and thresholds would be set initially during pre-launch to allow all data to pass through. After launch, these numbers shall be adjusted accordingly based on operational experiences.

7. TDR to SDR Conversion

As a cross-track scanning microwave radiometer, pure vertical (V) or horizontal (H) polarization measurements of ATMS only occur at the nadir direction. At other scan angles, the measurements represent a mixed contribution from both V and H polarizations. Thus, it is necessary to define the quasi-vertical and quasi-horizontal antenna brightness temperatures (TDR), T_a^{Qv} and T_a^{Qh}, which are defined as,

$$T_a^{Qv} = T_a^v \cos^2 \theta + T_a^h \sin^2 \theta \tag{30}$$

$$T_a^{Qh} = T_a^v \sin^2 \theta + T_a^h \cos^2 \theta \tag{31}$$

where T_a^v and T_a^h are the antenna brightness temperatures of the vertically polarized and horizontally polarized components, respectively, following the conventional definition. θ is the scan angle from nadir. This is an approximation derived from the general Stokes vector transformation with an assumption of zero third and fourth Stokes components. Thus, the ATMS antenna receives a linear combination of the pure vertical and horizontal components.

Moreover, considering the radiations from the Earth, cold space and satellite platform entering through the antenna main and side lobes in terms of corresponding antenna beam efficiencies, the two, T_a^{Qv} and T_a^{Qh} can be expressed as (Weng et al., 2012 and Weng et al., 2013):

$$T_a^{Qv} = (\eta_{me}^{vv} + \eta_{se}^{vv})T_b^{Qv} + (\eta_{me}^{hv} + \eta_{se}^{hv})T_b^{Qh} + \eta_{sc}T_{c,RJ} + S_a^{Qv} \tag{32}$$

$$T_a^{Qh} = (\eta_{me}^{hh} + \eta_{se}^{hh})T_b^{Qh} + (\eta_{me}^{vh} + \eta_{me}^{vh})T_b^{Qv} + \eta_{sc}T_{c,RJ} + S_a^{Qv} \tag{33}$$

where η_{me}^{vv} and η_{me}^{hh} are the co-polarized antenna main beam efficiency; η_{me}^{vh} and η_{me}^{hv} are the cross-polarized antenna main beam efficiency; η_{se}^{vv} and η_{se}^{hh} are the co-polarized antenna side lobe beam efficiency; η_{se}^{hv} and η_{se}^{vh} are the cross-polarized antenna side lobe beam efficiency; η_{sc} is the antenna side-lobe efficiency for the cold space; T_b^{Qv} and T_b^{Qh} are the quasi-V and quasi-H sensor brightness temperatures (SDR); and S_a^{Qv} and S_a^{Qh} are considered as the radiation contributions from the antenna near-field side-lobe or other effects such as the emitted radiation from ATMS flat reflector, and are handled by the scan bias correction.

Because ATMS does not provide pairs of perpendicular polarization channels, to correct antenna pattern, the perpendicular polarized antenna brightness temperature has to be estimated. For a given scan angle θ and a given surface conditions, there is a simple empirical relation between T_b^{Qv} and T_b^{Qh}:

$$T_b^{Qh} = A^h(\theta)T_b^{Qv} \tag{34}$$

$$T_b^{Qv} = A^v(\theta)T_b^{Qh} \tag{35}$$

where $A^h(\theta)$ and $A^v(\theta)$ are functions depending on the scan angle.

It should be noted that maximum cross-polarization contribution occurs when the ATMS views a cloudless dry atmosphere over calm ocean surface. The cross-polarization term is only significant over ocean for surface sensitive channels. Therefore, $A(\theta) = 1$ for temperature and water vapor sounding channels.

Applying Eqs. 34-35 in Eqs. 32-33 yields

$$T_b^{Qv} = \left(T_a^{Qv} - \eta_{sc}T_{c,RJ} - S_a^{Qv}\right)/[\eta_{me}^{vv} + \eta_{se}^{vv} + A^h(\eta_{me}^{hv} + \eta_{se}^{hv})] \tag{36}$$

$$T_b^{Qh} = \left(T_a^{Qh} - \eta_{sc}T_{c,RJ} - S_a^{Qh}\right)/[\eta_{me}^{hh} + \eta_{se}^{hh} + A^v(\eta_{me}^{vh} + \eta_{se}^{vh})] \tag{37}$$

Finally, the scan bias correction model has following forms:

$$S_a^{Qv} = \beta_0^v + \beta_1^v sin^2\theta \tag{38}$$

$$S_a^{Qh} = \beta_0^h + \beta_1^h cos^2\theta \tag{39}$$

where β_0^v, β_1^v β_0^h and β_1^h are the coefficients obtained from fitting the on-orbit ATMS pitch-maneuver data. Eqs 36-37 can also be written as

$$T_b^{Qv} = a^v(\theta)T_a^{Qv} + b^v(\theta) \tag{40}$$
$$T_b^{Qh} = a^h(\theta)T_a^{Qh} + b^h(\theta) \tag{41}$$

The slope and intercept for TDR to SDR conversion are derived as

$$a^v(\theta) = 1.0/\left[\eta_{me}^{vv} + \eta_{se}^{vv} + A^h(\eta_{me}^{hv} + \eta_{se}^{hv})\right] \tag{42a}$$

$$b^v(\theta) = -\left(\eta_{sc}T_{c,RJ} + S_a^{Qv}\right)/\left[\eta_{me}^{vv} + \eta_{se}^{vv} + A^h(\eta_{me}^{hv} + \eta_{se}^{hv})\right] \tag{42b}$$

$$a^h(\theta) = 1.0/\left[\eta_{me}^{hh} + \eta_{se}^{hh} + A^v(\eta_{me}^{vh} + \eta_{se}^{vh})\right] \tag{43a}$$

$$b^h(\theta) = -\left(\eta_{sc}T_{c,RJ} + S_a^{Qh}\right)/\left[\eta_{me}^{hh} + \eta_{se}^{hh} + A^v(\eta_{me}^{vh} + \eta_{se}^{vh})\right] \tag{43b}$$

8. Remap Sensor Brightness Temperature

As one of the key instrument suites on the Suimi NPP satellite the Cross-track Infrared and Microwave Sensor Suite (CrIMSS) consists of the Cross-track Infrared Sounder (CrIS) and the Advanced Technology Microwave Sounder (ATMS). The primary purpose of CrIMSS is to produce measurements of the atmospheric temperature and moisture profiles to support weather forecasting applications. While the high spectral resolution of the CrIS instrument enables accurate retrieval of atmospheric temperature and moisture profiles with high vertical and horizontal resolutions, the microwave instrument ATMS provides a stable initialization for the retrieval of the atmospheric profiles from infrared data when only minor cloud obstruction is present as well as a backup data product when substantial cloud is present which prevents a successful retrieval using infrared data.

One basic requirement that enables the synergistic use of CrIS and ATMS measurements is that the footprints of the two instruments must cover nearly identical area on the Earth's surface. Such a requirement for a common footprint is met by the production of the remapped ATMS brightness temperature which is a spatially resampled ATMS brightness temperature measurement. The remapped ATMS brightness temperature is the optimal estimation of the Earth's brightness temperature over an idealized area overlapping the CrIS' footprint using several nearby ATMS measurements. The widely used resampling approach was often referred to as the Backus-Gilbert approach (Backus and Gilbert, 1970). The adaptation of the Backus-Gilbert method for the resampling of microwave measurement was proposed and analyzed to Special Sensor Microwave Imager (SSM/I) (Poe, 1990).

During the normal operation of ATMS, the instrument performs three cross orbit track scans from -52.7 to 52.7 degree relative to nadir in a continuous motion every 8 seconds. For a single scan, ATMS instrument takes 96 measurements of microwave radiances at evenly spaced time intervals. The Fields of Regards (FOR) of each of these measurements are nearly circular with different nominal radii for different channels. Synchronized every 8 seconds to ATMS, the CrIS instrument performs a single cross-track scan during this time interval. However, CrIS operates in a step-and-stare mode with a total of 30 sub-orbital stare periods, also referred to as Fields of Regards. During each stare period, the instrument provides compensation for the along the track motion of the spacecraft to ensure that the footprints of the instrument on the Earth's surface are nearly immobile. With its nine detectors, often referred to as nine Fields of View (FOV), for each of its three spectral bands, the CrIS instrument collects 27 interferograms per FOR. A nominal geometric arrangement of the ATMS and CrIS footprints is shown in Fig. 11.
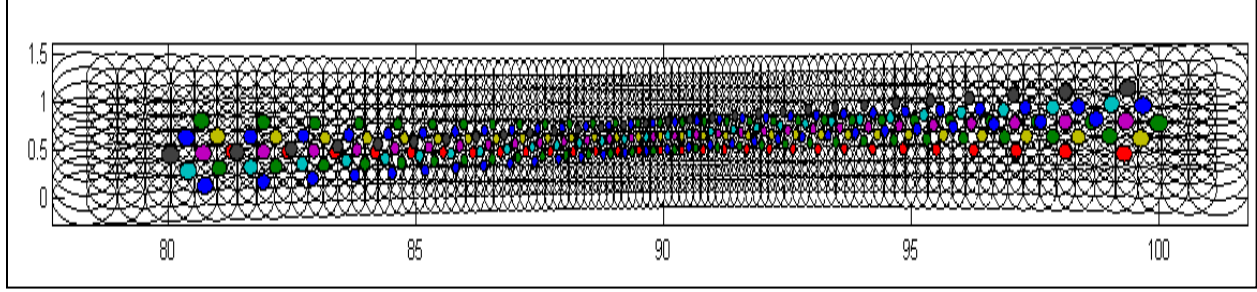
Figure 11. Arrangement of ATMS and CrIS footprints is shown with solid black lines for ATMS footprints and the colored circles representing the 9 different FOVs of CrIS.

The purpose of producing the remapped ATMS brightness temperature or radiance is to construct an accurate representation of microwave radiances for the region covered by a footprint of CrIS using nearby measured ATMS radiances.. Corresponding to each CrIS FOR, the remapped ATMS radiances has the form

$$T_b^r = \sum_{k=1}^{n} \alpha_k T_{b,k} \tag{44}$$

where the composite radiances R_c is simply a weighted sum of the native ATMS radiances R_k. The weights α_k for all CrIS FORs and ATMS channels are determined to optimize the accuracy of the representation of the microwave radiances over the CrIS footprint.

An accurate characterization of the native footprints of the instrument including its location and its shape on the Earth's surface is essential for the generation of the remapped ATMS radiance or brightness temperature. This characterization requires a precise knowledge of the relative alignment of the two instruments, the synchronization of their scanning mechanism, as well as the gain patterns for all channels. Prior to the launch of the Suomi NPP satellite, the boresight alignment relative to the instrument reference frame and the beam width and efficiency of the antenna for a representative set of channels are measured during the antenna subsystem test. Both the beam width and the antenna efficiency are derived from the measurement of the antenna gain pattern. For each view direction identified by its zenith angle φ and azimuth angle θ relative to the boresight of the antenna and in-track direction, the antenna gain $\rho(\theta, \varphi)$ is defined as the ratio between the measured radiance and the scene radiance from the given direction.

The measured brightness temperature or radiance can be represented as follows:

$$T_{b,k} = \iint_{\Omega} T_b(\vec{x}) \rho_k(\vec{x}) dA \tag{45}$$

where Ω represents the region in the field of regard of the instrument, $T_b(\vec{x})$ corresponds to the radiance at location $\vec{x}$ inside of the field of regard and,

$$\rho_k(\vec{x}) = \rho(\theta_k(\vec{x}), \varphi_k(\vec{x})) \sin(\eta_k(\vec{x})). \tag{46}$$

The zenith angle $\boldsymbol{\theta}_k(\vec{\boldsymbol{x}})$ and the azimuth angle $\boldsymbol{\varphi}_k(\vec{\boldsymbol{x}})$ of the location $\vec{\boldsymbol{x}}$ in the antenna field of regard and the elevation angle $\boldsymbol{\eta}_k(\vec{\boldsymbol{x}})$ of the satellite are all functions of the scene selection mirror angle for the $\boldsymbol{k}$-th FOR and the position of the satellite. The effective spatial response function for the remapped ATMS radiance T_b^c is given by

$$\rho_c(\vec{x}) = \sum_{k=1}^{n} \alpha_k \, \rho_k(\vec{x}). \tag{47}$$

If the standard deviation of a radiance measurement is σ^2, the variance of the remapped ATMS radiance is given by

$$\sigma_c^2 = \sigma^2 \sum_{k=1}^{n} \alpha_k^2. \tag{48}$$

The Backus-Gilbert method of remapping consists of minimizing the following function

$$\cos^2 \beta \int_{\Omega} |\rho_c(\vec{x}) - \rho_0(\vec{x})|^2 \, dA + \sin^2 \beta \sum_{k=1}^{n} \alpha_k^2, \tag{49}$$

over all possible selections of the weights α_k subject to the following constraint

$$\sum_{k=1}^{n} \alpha_k = 1.$$

The reference spatial response function $\rho_0(\vec{x})$ represents the desired spatial response function for CrIS which is a Gaussian function.

As it is indicated early, the zenith angle $\theta_k(\vec{x})$ and azimuth angle $\varphi_k(\vec{x})$ in the antenna field of regard of the location $\vec{x}$ on the Earth's surface and the elevation angle $\eta_k(\vec{x})$ of the satellite are all functions of the scene selection mirror angle for the k-th FOR and the position of the satellite at the time. Therefore, the computation of these angles requires simulation of the satellite motion, the synchronization of the scanning mechanisms between CrIS and ATMS, as well as the relative alignment of the two instruments. The relative alignment of the two instruments was measured during the integration process of the Suomi NPP satellite. The measured alignment information for each of the two instruments relative to the nominal spacecraft nadir used in the training of the resampling coefficients is obtained during the spacecraft integration test. While the alignments of the instrument obviously affect the relative positions of the footprints, the motion of the satellite and the synchronization of the scans also play important role.

In order to make the remapping algorithm computationally efficient, it is determined that the accuracy of the resampled radiance can be achieved by using a set of coefficients α_k that depends only on the corresponding CrIS FOR and is independent of the position of the satellite. Therefore, we must make the *Earth Centered Inertia (ECI) frame* and *spherical Earth* assumption. In the training of the resampling coefficients, the instrument footprints are projected on a spherical surface in the ECI frame. This implies that the Earth's surface is approximated by a spheric surface and the Earth's rotation is not considered. These approximations make the resampling coefficients independent of the latitude of the satellite and the ascending and descending portion of the orbit.

It is interesting to note that the synchronization of the CrIS and ATMS scans in time can affect the relative position of their footprints in the along-track direction due to the motion of the satellite. Under nominal operation conditions, ATMS and CrIS are synchronized every eight seconds at the beginning of the integration interval of the first field of regard (FOR). An important factor to consider is the integration interval for each FOR. In the case of ATMS, the consecutive FORs are separated by 0.018 seconds with 95% of this interval being the integration interval. On the other hand, the FORs for CrIS are separated by 0.2 seconds with an integration interval of 0.17 seconds.

Another detail that is considered in the training of the resampling coefficients is the fact that ATMS operates in continuous scan mode. That is, the cross-track scanning motion is continuing during the time interval for measuring the Earth scene radiances. As a result, the rapid motion of scanning mirror has the effect of elongating the footprint of the FOR. In order to account for this effect, we approximate the elongated footprint by the sum of a set of five evenly spaced instantaneous antenna pattern. The elongation of the ATMS footprint due to the continuous scanning motion during integration interval is quite significant. On the other hand, since CrIS operates in a step-and stare mode with along-track motion compensation, we consider its footprint to be stationary during the 0.17-second integration interval.

Following the optimization process, we obtain an estimation of the difference between the optimized composite sensor response $\rho_c(\vec{x})$ and the reference response $\rho_0(\vec{x})$, as well as, an estimate for the noise reduction factor.

9. References

Anderson, K., 2004: ATMS SDR Algorithm Description; NGES TM-01-380D

Backus, G., and F. Gilbert, 1970: Uniqueness in the Inversion of Inaccurate Gross Earth Data, *Phil. Trans. R. Soc. Lond.,* 266, 123-192

Blackwell, W. J. and F. W. Chen: 2005: SDR Impact of Known CrIMSS Yaw Rotation Offsets, MIT Lincoln Laboratory

Poe, G. A., 1990: Optimum Interpolation of Imaging Microwave Radiometer Data, *IEEE Trans. Geosci. Remote Sens.*, 28, 800-810

Weng, F., X. Zou, N. Sun, H. Yang, M. Tian, W.J. Blackwell, X. Wang, L. Lin, and K. Anderson, 2013: Calibration of Suomi National Polar-Orbiting Partnership (NPP) Advanced Technology Microwave Sounder (ATMS), *J. Geophys. Res.* Atmos., **118**, 1–14, doi:10.1002/jgrd.50840

Weng, F., H. Yang, and X. Zou, 2012: On Convertibility from Antenna to Sensor Brightness Temperature for Advanced Technology Microwave Sounder (ATMS*), IEEE Geosci. Remote. Sens. Letter,* 10.1109/LGRS.2012.2223193

Weng, F. and X. Zou, 2013: Errors from Rayleigh–Jeans Approximation in Satellite Microwave Radiometer Calibration System, *Appl. Optics*, 12, 505-508.